

## Influence of chemisorbed oxygen on the growth of europium phases on V(110)

T. Gourieux,\* S. Fréchar, F. Dulot, J. Eugène, B. Kierren, and D. Malterre

*Laboratoire de Physique des Matériaux, Université Henri Poincaré, Nancy I—Boîte Postale 239, F-54506 Vandœuvre-lès-Nancy, France*

(Received 21 January 2000)

A structural and spectroscopic study of Eu exotic phases grown on V(110) reveals the large influence of chemisorbed oxygen on the growth process. While hexagonal Eu layers are obtained on a clean  $(1 \times 1)$ -V(110) surface, three-dimensional (3D) growth of pure Eu fcc islands is induced by the presence of the oxygen- $c(6 \times 2)$  surface reconstruction of V(110). A detailed analysis shows that this Eu phase exhibits a 9.5% reduction of the first-neighbor distance with respect to the bcc phase. In both cases (2D and 3D growth of Eu), singular Eu 4*d* photoemission spectra are observed.

### I. INTRODUCTION

Elaboration of materials with reduced dimensions often leads to the observation of new physical properties as compared to the bulk, such as modification of Curie temperatures, exotic crystallographic phases, or quantum size effects due to electron confinement. Key points in the preparation of a particular nanomaterial by the molecular beam technique lie in the choice of a substrate as well as its temperature and surface quality. This is because the nucleation process is driven by physical parameters (surface adatom mobility and Gibbs free energies) which are directly dependent on these initial conditions. Therefore, besides its temperature dependence, the growth can be seriously altered by strains resulting from lattice mismatch, or by the initial presence of surface defects as well as surface reconstructions.<sup>1</sup> It can also be affected by the initial presence of chemisorbed species. For instance, it has been recently shown that the O- $(1 \times 1)$  phase on Fe(100) acts as a surfactant for homoepitaxy.<sup>2</sup> It will be shown in this paper that chemisorbed oxygen can completely change the growth process so that the resulting nano-objects have new physical properties. This will be demonstrated for the specific problem of rare earth (RE) epitaxial growth on transition metals (TM's) in the particular case of the Eu/V(110) interface, by using the possibility of realizing either a  $(1 \times 1)$ -V(110) surface corresponding to the crystal bulk termination, or an oxygen induced  $c(6 \times 2)$  reconstruction of this surface.

Thin film epitaxy of RE's on the (110) faces of the first bcc TM's (V and Cr columns) has been experimentally demonstrated during the last 20 years.<sup>3-10</sup> The crystal symmetry adopted by these RE films generally accords with the bulk natural phases, which consist in a stacking of hexagonal planes leading to cfc, hcp, double hcp (dhcp), or Sm-type structures. The RE lattice matches that of the TM(110) following the so-called Nishiyama-Wassermann (NW) orientation, for which the most densely packed rows of the hexagonal RE plane are parallel to the densely packed [001] rows of the TM [see Fig. 1(a)]. However, due to the large discrepancy between the lattice parameters, epitaxy occurs by matching *m* RE rows with *n* TM rows defining an *m*:*n* epitaxy, *m* and *n* depending on both the RE and the TM.<sup>3,7</sup> Up to now, this behavior applies to all the RE's studied, but one has to pay attention to the particular case of Eu. Indeed, this

element crystallizes in a bcc phase whereas hexagonal epitaxial Eu on TM(110) surfaces have been reported.<sup>11,12</sup> In the case of Eu/W(110),<sup>11</sup> hexagonal Eu structures with various expanded surface parameters appear in the submonolayer range following the NW orientation, but thicker Eu coverages were not studied. For Eu/Ta(110),<sup>12</sup> similar hexagonal structures were observed in the submonolayer range. At higher coverages epitaxy of hexagonal Eu planes starting with the NW orientation is observed, but then switching to the Kurdjumov-Sachs (KS) orientation [i.e., a rotation by 5° relative to the NW orientation; see Fig. 1(a)], and finally reaching bcc Eu(110) domains with [001] rows parallel to the Ta[001] rows.

The experimental study we report concerns the deposition of Eu thin films on a V(110) substrate studied by reflection high energy electron diffraction (RHEED), scanning tunneling microscopy (STM), and x-ray photoemission spectroscopy (XPS) measurements. The motivations were twofold, first, starting from the bulk lattice parameters of bcc Eu and V ( $a_V = 3.027 \text{ \AA}$ ,  $a_{Eu} = 4.5827 \text{ \AA}$ ),<sup>13</sup> there is a geometrical possibility that the lattice matching occurs by alignment of the densely packed [001] rows, realizing a 2:3 epitaxy [see Fig. 1(b)]. This had to be tested and compared with previous works on W and Ta substrates. Second, we took advantage of the well known oxygen induced  $c(6 \times 2)$  reconstruction of the V(110) surface<sup>14,15</sup> in order to study its influence on the Eu growth. This also gives the opportunity to investigate the influence of the crystallographic structure on the spectroscopic properties of Eu. The presentation and discussion of the experimental results are organized as follows. Section II deals with a survey of experimental details and a brief description of the substrate preparation. Section III reports on the structural results including a detailed analysis of RHEED patterns obtained in the three-dimensional (3D) growth phase of Eu in the presence of the O- $c(6 \times 2)$  V(110) reconstructed surface. Section IV is a preliminary report of our photoemission results, which will detail the chemical nature of these 3D islands as well as the singular Eu 4*d* XPS line shapes we obtained.

### II. EXPERIMENTAL DETAILS AND SUBSTRATE PREPARATION

Experiments have been performed in an UHV system with a base pressure better than  $5 \times 10^{-10}$  mbar. 99.9% pure

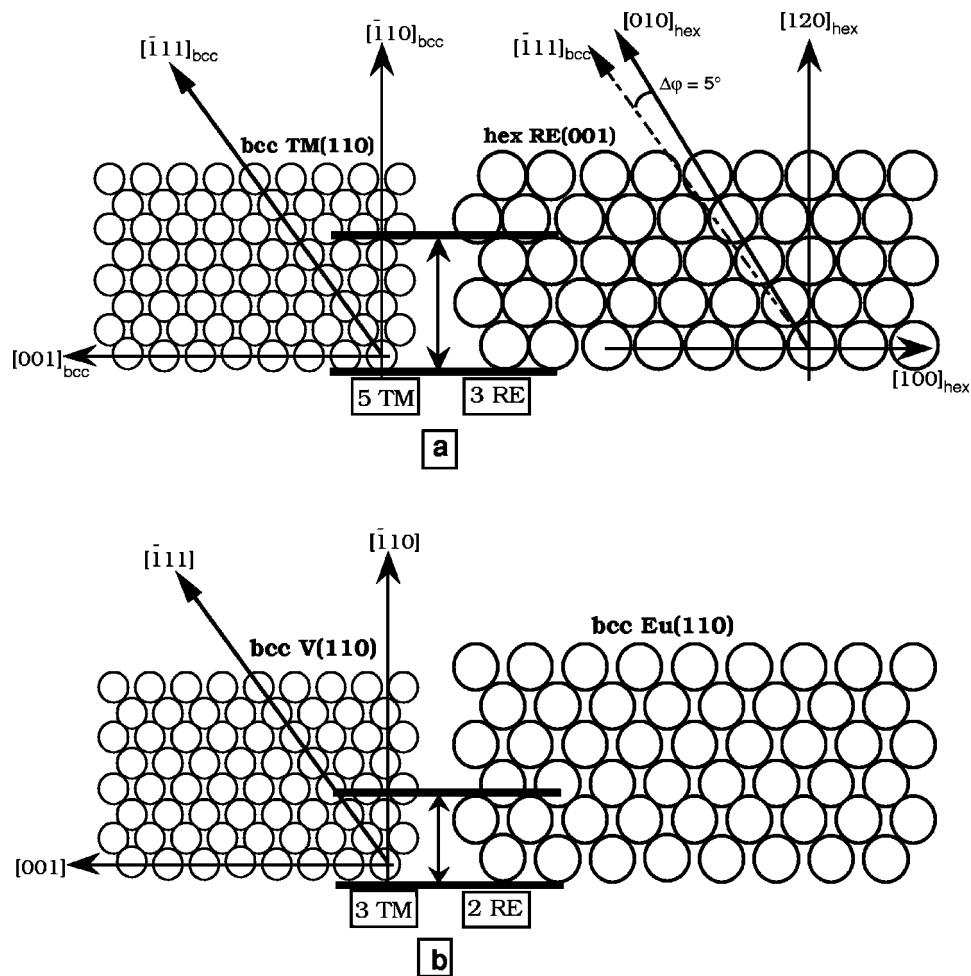


FIG. 1. (a) Nishiyama-Wassermann 3:5 epitaxy of hexagonal Eu layers on V(110). The TM(110) axis are indexed following the usual bcc cubic notation while, for convenience, indexing of the Eu layer axis follows the hexagonal ( $abc$ ) notation. Kurdjumov-Sachs epitaxy occurs when the  $[\bar{1}11]_{\text{bcc}}$  axis is aligned with the  $[010]_{\text{hex}}$  axis (or an equivalent one). Thus, there is a  $5^\circ$  switching between NW and KS orientations. The drawing is adapted from Ref. 7. (b) Expected geometrical 2:3 epitaxy of bcc Eu(110) on V(110) with alignment of  $[001]$  rows.

Eu was sublimated from a boron nitride effusion cell and the deposited nominal thicknesses were continuously measured with a water-cooled quartz oscillator placed in the vicinity of the V(110) substrate. RHEED experiments were performed both during and after the growth by using a VG LEG 300 gun electron tuned to 30 keV. An UHV mechanical transfer allowed us to carry out either STM or XPS measurements on the same sample. The XPS measurements were performed with a VG MK II analyzer using a nonmonochromatized Al  $K\alpha$  source (overall resolution 1 eV). STM measurements were carried out by using an Omicron STM 1 apparatus operating at room temperature in the constant current mode.

The V(110) single crystal surface was prepared by the usual  $\text{Ar}^+$  ion bombardments and annealings at various temperatures  $T_A$ . Depending on  $T_A$ , this operative mode led to either a  $(1 \times 1)$ -V(110) surface corresponding to the crystal bulk termination, or a  $c(6 \times 2)$  reconstructed surface induced by oxygen diffusion from the bulk. The  $(1 \times 1)$ -V(110) surface was obtained for  $T_A$  values around  $350$ – $400^\circ\text{C}$ . STM images of this surface displayed a succession of relatively small terraces forming hills and valleys at large lateral scale (about 100 nm). XPS revealed that it was free of impurities.

This kind of surface gave rise to streaky RHEED patterns of good quality, as shown in Figs. 2(a) and 2(b). These experimental patterns are in agreement with the expected ones for a bcc(110) plane within an overall error of 2% for both angular spacings and distance ratios. Therefore, they were chosen as a reference for the distance calibration.

By increasing  $T_A$ , oxygen impurities diffuse from the bulk inducing the  $\text{O}-c(6 \times 2)$  surface reconstruction of V(110).<sup>14,15</sup> This thermodynamical process was activated as soon as  $T_A$  was set higher than  $450^\circ\text{C}$ , which is the same limiting value as in the case of Nb(110).<sup>16</sup> As observed by STM, it led to larger terraces (mean width  $200 \text{ \AA}$  for  $T_A = 600^\circ\text{C}$ ) with monoatomic steps. Atomic resolution STM images revealed the  $c(6 \times 2)$  reconstruction with a unit mesh adopting two preferential orientations in such a manner that the whole surface looked like a kind of checkerboard at a mesoscopic scale.<sup>17</sup> RHEED was poorly sensitive to these details showing only more or less visible fractional order streaks at the expected  $\frac{1}{3}$  positions for the  $[\bar{1}11]_{\text{V}}$  and  $\frac{1}{2}$  positions for the  $[\bar{1}10]_{\text{V}}$  azimuth [see Figs. 3(a) and 3(b)]. Carbon impurities were sometimes observed by XPS for high annealing temperatures ( $T_A \geq 600^\circ\text{C}$ ). Thus, for this

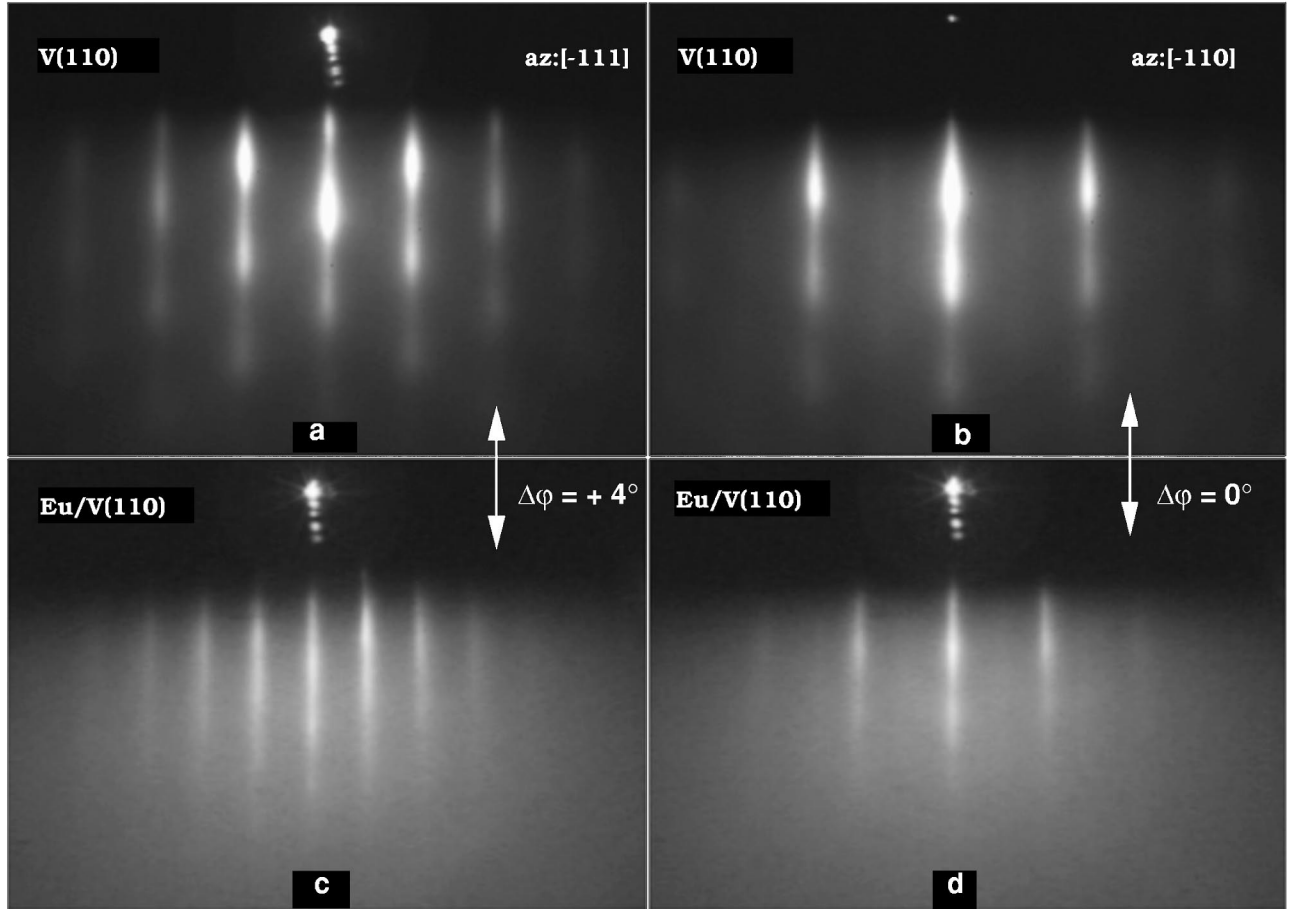


FIG. 2. (a) and (b) RHEED patterns of  $(1 \times 1)$ -V(110) for the two azimuths  $[\bar{1}11]$  and  $[\bar{1}10]$ . Experimental angular spacing between these two azimuths is  $35^\circ$ . (c) and (d) RHEED patterns obtained after the deposition of  $38 \text{ \AA}$  Eu on  $(1 \times 1)$ -V(110) at  $T_S = 260^\circ\text{C}$ . Note the experimental angular spacings  $\Delta\varphi = +4^\circ$  between patterns (a) and (c), and  $\Delta\varphi = 0^\circ$  between patterns (b) and (d); these are consistent with a NW orientation of the Eu film (see Fig. 1).

study, the  $T_A$  value was limited to  $450\text{--}500^\circ\text{C}$  in order to avoid carbon contamination.

To summarize this section, we were able to prepare two distinct substrate surfaces: for  $T_A$  values in the range  $350\text{--}400^\circ\text{C}$  the  $(1 \times 1)$ -V(110) surface was identified (referred to as substrate  $S_{1 \times 1}$  in the following), while in the range  $450\text{--}500^\circ\text{C}$  the oxygen induced  $c(6 \times 2)$  surface reconstruction was initiated (referred to as substrate  $S_{c(6 \times 2)}$ ).

### III. STRUCTURE RESULTS

During the Eu evaporation, the substrate ( $S_{1 \times 1}$  or  $S_{c(6 \times 2)}$ ) was held at a temperature  $T_S$  chosen in the range  $25\text{--}260^\circ\text{C}$ . The lower value was a technical limitation of the experimental setup, while the upper one resulted from the experimental observation that setting  $T_S$  at a higher value led to the desorption of deposited Eu atoms. This behavior was not very surprising because of the particularly low heat of sublimation of this element ( $\approx 1.5 \text{ eV/atom}$  under normal conditions) which leads to high vapor pressure values even at moderate temperatures (e.g.,  $10^{-5}$  mbar at  $400^\circ\text{C}$ ).

For  $T_S < 260^\circ\text{C}$ , 2D growth occurred using either  $S_{1 \times 1}$  or  $S_{c(6 \times 2)}$ , differing only in details as observed in RHEED. But for  $T_S \approx 260^\circ\text{C}$ , the Eu growth was found to strongly depend on the substrate: 2D growth was persistent on  $S_{1 \times 1}$ ,

while 3D islands formed on  $S_{c(6 \times 2)}$ . In the following, we will first emphasize the 2D growth case.

#### A. Bidimensional growth of Eu

For  $T_S < 260^\circ\text{C}$ , and using  $S_{1 \times 1}$  or  $S_{c(6 \times 2)}$ , Eu deposits in the submonolayer range only induced an increasing background on the RHEED patterns with no evidence of ordered structure formation. Then, near the monolayer, additional streaks of weak intensity started to develop in the RHEED patterns, demonstrating the bidimensional nature of the Eu growth. These streaks increased in intensity for higher Eu coverages while the substrate signature disappeared, giving rise to the RHEED patterns shown in Figs. 2(c) and 2(d). They reveal a Eu surface lattice with hexagonal symmetry and parameter  $a_s = 4.1 \pm 0.1 \text{ \AA}$ . The angular differences  $\Delta\varphi$  quoted in Fig. 2 are consistent with a NW orientation of the Eu film, the result being a 3:5 epitaxy as drawn in Fig. 1(a). Eu films were hexagonal up to a critical thickness (a few tens of angstroms) which was  $T_S$  dependent. Films of best quality (as seen in RHEED) were obtained on  $S_{1 \times 1}$  at  $T_S = 260^\circ\text{C}$ . Increasing the film thickness led to various alterations of the diffraction patterns, like streak broadening, background enhancement, and persistence of the diffraction patterns when varying the azimuthal angle over about  $10^\circ$  (i.e., texture formation). These changes were temperature ( $T_S$ ) and thickness

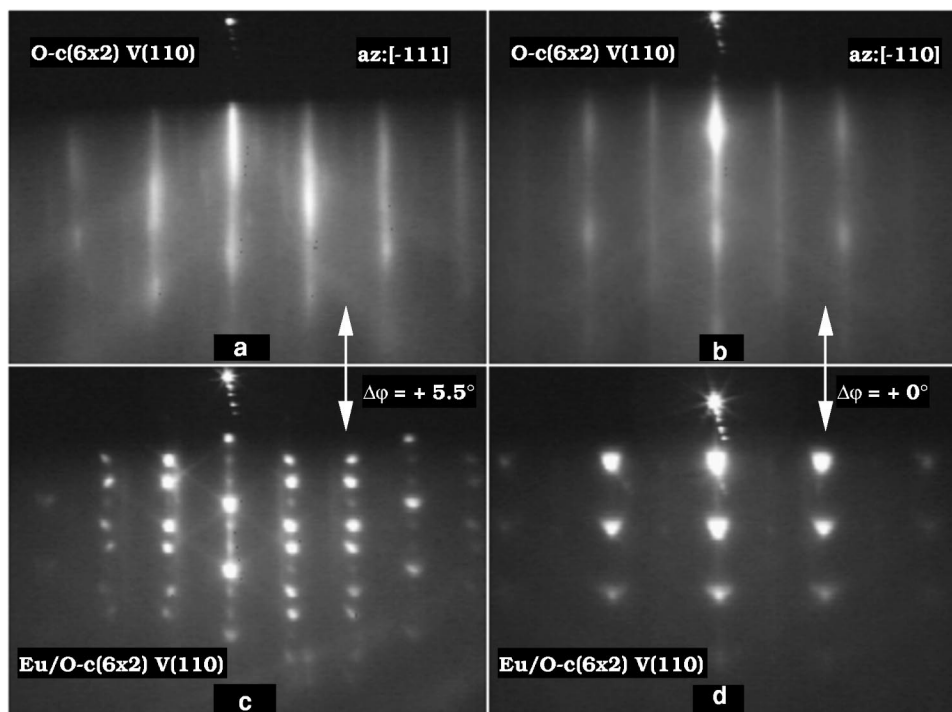


FIG. 3. (a) and (b) RHEED patterns of the oxygen induced  $c(6 \times 2)$ -V(110) surface for the two azimuths  $[\bar{1}11]$  and  $[\bar{1}10]$ . (c) and (d) Spotty RHEED patterns obtained after the deposition of  $8.4 \text{ \AA}$  Eu on the  $c(6 \times 2)$ -V(110) reconstructed surface at  $T_S = 260 \text{ }^\circ\text{C}$ . The corresponding STM image is reported in Fig. 4(a) below. The quoted angular spacings  $\Delta\phi$  indicate a NW orientation of the islands relative to the V(110) lattice, while the spot distribution agrees with a fcc structure (see text).

dependent, and are believed to be related to the relaxation of the Eu hexagonal layers (3:5 epitaxy) toward bcc Eu(110) (2:3 epitaxy). This requires as a final result a  $5^\circ$  rotation of the Eu surface lattice (see Fig. 1) and a slight variation of the Eu first-neighbor distance ( $4.12 \text{ \AA}$  for the 3:5 epitaxy compared with  $3.97 \text{ \AA}$  in the bcc phase). This high coverage behavior was clearly identified for  $T_S = 25 \text{ }^\circ\text{C}$ , where the final bcc Eu film ( $100 \text{ \AA}$ ) was observed to follow the ‘‘natural’’ 2:3 epitaxy as indicated in Fig. 1(b).

### B. Tridimensional growth of Eu on the O- $c(6 \times 2)$ V(110) reconstructed surface

We turn now to the description of the 3D Eu phase we encountered at  $T_S = 260 \text{ }^\circ\text{C}$  on  $S_{c(6 \times 2)}$ . After an initial background enhancement, high intensity diffraction spots appeared on the RHEED patterns revealing a 3D growth process as soon as a nominal Eu thickness of one monolayer was deposited [Figs. 3(c) and 3(d)]. Interpretation of these spotty diffraction patterns was greatly facilitated by STM measurements (Fig. 4). At a mesoscopic scale, the nanoparticles revealed a threefold symmetry, their mean shape being truncated tetrahedrons with height ( $H$ ) and base ( $B$ ) depending on the deposited Eu thickness. With increasing nominal thickness an increase in both island density and  $B/H$  ratio was first observed (see the profiles in Fig. 4). Higher Eu deposition led to the formation of a poorly ordered bcc Eu film (as observed in RHEED), probably growing on top of the 3D islands as well as in between.

It can be seen on Fig. 4 that some of the 3D islands are  $60^\circ$  twinned (marked  $I1$  and  $I2$  on Fig. 4), showing the existence of two equivalent epitaxial orientations. This is of

importance for the interpretation of the RHEED patterns of Fig. 3 because they result from diffraction by transmission across these two kinds of islands. In possession of this information, the following method was then used for the 3D crystal structure determination of these islands. First, and consistent with the threefold symmetry observed in STM, it was verified that the observed azimuthal angles led to a hexagonal lattice in the plane of growth following the NW orientation (see the  $\Delta\phi$  values quoted in Fig. 3). The in-plane parameter was then deduced from the horizontal spot spacings,  $a = 3.59 \pm 0.07 \text{ \AA}$ . These  $\Delta\phi$  and  $a$  values imply a hexagonal 2:3 epitaxy relative to the V(110) lattice. Then, advantage was taken of the following 3D diffraction property: depending on the azimuth, a periodic stacking of  $n$  distinct hexagonal planes ( $A$ ,  $B$ , or  $C$  type) leads to  $(001), (002), \dots, (00n-1)$  spot extinction along the so-called central rod, while  $n$  fractional order spots can switch on in the neighboring rods.<sup>18</sup> Leaving out at first the presence of low intensity spots, the case  $n = 3$  (i.e.,  $ABC$  stacking) can be recognized when looking at the diffraction pattern of Fig. 3(c). Then, assuming this kind of stacking and starting from a hexagonal lattice description, it was possible to simulate all the observed RHEED patterns. As can be seen in Fig. 5, it was necessary to take into account the  $60^\circ$  twinned islands in order to reproduce the experimental patterns. Thus, Fig. 3(c) results from the superposition of two diffraction patterns arising from the two nonequivalent  $[100]$  and  $[110]$  azimuths,  $60^\circ$  rotated (Fig. 5). In the same way, Fig. 3(d) appears as the superposition of two diffraction patterns arising from the two equivalent  $[210]$  and  $[1\bar{1}0]$  azimuths. The best fit to the data was obtained for a lattice parameter along the

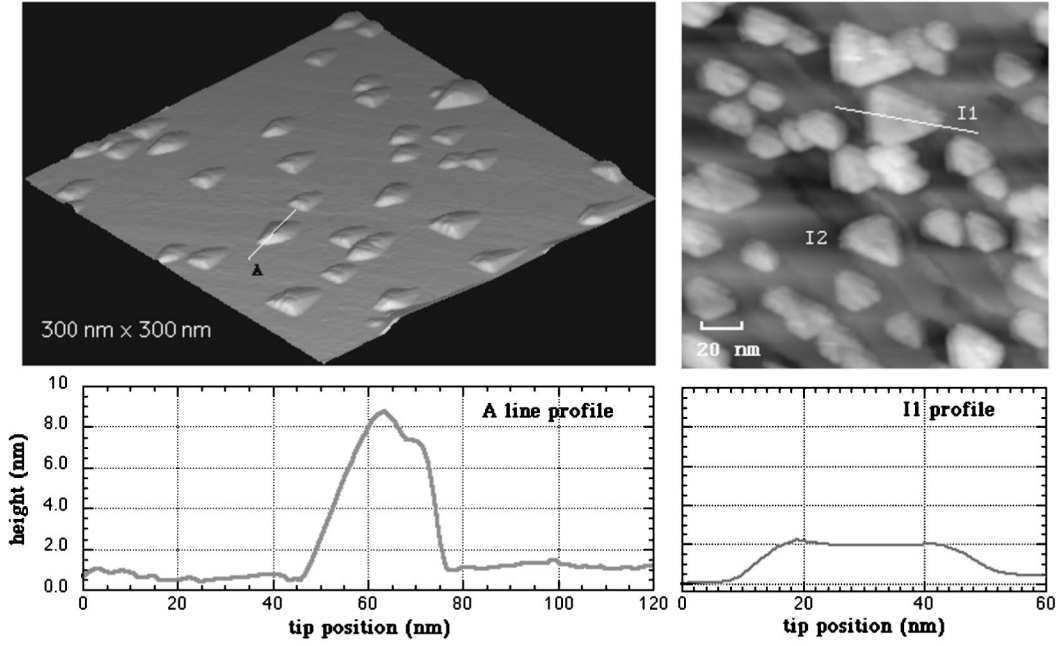


FIG. 4. (a)  $300 \text{ nm} \times 300 \text{ nm}$  STM image for an  $8.4 \text{ \AA}$  Eu nominal thickness deposited on substrate  $S_{c(6 \times 2)}$ . Gap voltage  $-0.08 \text{ V}$ , set point  $0.69 \text{ nA}$ . (b)  $180 \text{ nm} \times 180 \text{ nm}$  STM image for a  $9.5 \text{ \AA}$  Eu nominal thickness. Note the island height difference between the two images.

growth axis  $c = 9.06 \text{ \AA} = a\sqrt{6}$ . That is, the fcc structure occurs instead of a hexagonal  $ABC$  one (i.e.,  $c \neq a\sqrt{6}$ ). Using the cubic description of fcc crystals, the lattice parameter is then  $a_{\text{fcc}} = a\sqrt{2} = 5.1 \pm 0.1 \text{ \AA}$ .

Extra diffraction spots of lower intensity were clearly visible on some azimuths, which are not explained in the previous paragraph [see Figs. 3(c) and 5(c)]. These extra spots are commonly observed in transmission electron microscopy on fcc materials and mainly originate from double diffraction effects due to the presence of twinned nanoparticles.<sup>19</sup> That is, the diffracted beam arising from one nanoparticle becomes the incident beam for a neighboring one (Fig. 6). Let  $\vec{k}_0$  be the incident wave vector,  $\vec{k}_1 \equiv \vec{k}_0 - \vec{G}_1(h_1, k_1, l_1)$  a diffracted wave vector from the first nanoparticle, and  $\vec{k}_2 \equiv \vec{k}_1 - \vec{G}_2(h_2, k_2, l_2)$  the diffracted one resulting from a double diffraction on the second nanoparticle. If the second nanoparticle is  $60^\circ$  rotated, the double diffraction spot(s) must then be indexed as  $\vec{k}_0 - \vec{k}_2 \equiv \vec{G}(H = h_1 - k_2, K = k_1 + k_2 + h_2, L = l_1 + l_2)$  where the  $60^\circ$  rotated reciprocal lattice of the second nanoparticle has been taken into account. Thus, despite the same extinction conditions on  $(h_1, k_1, l_1)$  and  $(h_2, k_2, l_2)$ , they do not necessarily occur for  $(H, K, L)$ , depending on the original azimuth. For instance, in the case of the  $[100]$  azimuth of Fig. 3(c), the forbidden  $(00-2)$  spot switches on because of a double diffraction arising from  $\vec{k}_0 - \vec{k}_1 \equiv (-20-1)$  and  $\vec{k}_1 - \vec{k}_2 \equiv (2-2-1)$ . It was verified that all the extra spots observed on Fig. 3(c) could be explained according to this scheme. In the same way, extra spots were not observed on the diffraction pattern of Fig. 3(d) because it results from two equivalent azimuths in spite of the two different orientations of the nanoparticles; thus, in that case, the resulting  $(H, K, L)$  spots cannot generate new double diffraction spots.

## IV. PHOTOEMISSION RESULTS

### A. Chemical composition of the nanoparticles

An important question concerns the chemical composition of the 3D islands because of the initial presence of oxygen atoms on  $S_{c(6 \times 2)}$ , which leads one to suspect a chemical reaction with Eu atoms in order to form oxide nanoparticles. Two experimental observations might support this possibility. First, as said before, the 3D growth phase occurs only at  $T_S = 260^\circ \text{C}$  which could be interpreted as the temperature for which the oxidation process is activated. Such a Eu-O reaction has recently been reported by Konno *et al.*,<sup>20</sup> who obtained  $\text{EuO}_{1 \pm x}$  thin films by reactive evaporation on Si(100) wafers for  $T_S$  values as low as  $200^\circ \text{C}$ . However, an oxygen flow was present during these experiments while in our case the oxygen atoms are chemically bonded with the vanadium ones. The second observation is of crystallographic nature: both the fcc structure and the lattice parameter ( $5.1 \pm 0.1 \text{ \AA}$ ) we found for the nanoparticles compare well with those<sup>13</sup> of divalent europium oxide  $\text{EuO}$  ( $a_{\text{EuO}} = 5.14 \text{ \AA}$ ).

In order to give an unequivocal answer to this question, an estimation of the oxygen quantity present on the sample was carried out with the help of photoemission measurements before and after Eu evaporation. Figures 7(b) and 7(c) present the V  $2p$  and O  $1s$  spectra for the two situations. Estimation of the O  $1s$  line intensities required special treatment because of its smallness and because of the presence of a broad V  $2p$  satellite lying at the same energy [see Fig. 7(a)]. In order to overcome this difficulty, we removed the V  $2p$  line of a freshly ion bombarded V(110) surface from other spectra. This procedure was quite satisfactory and line intensities were then calculated in this way after the subtraction of a Shirley-type background. It was found that the in-

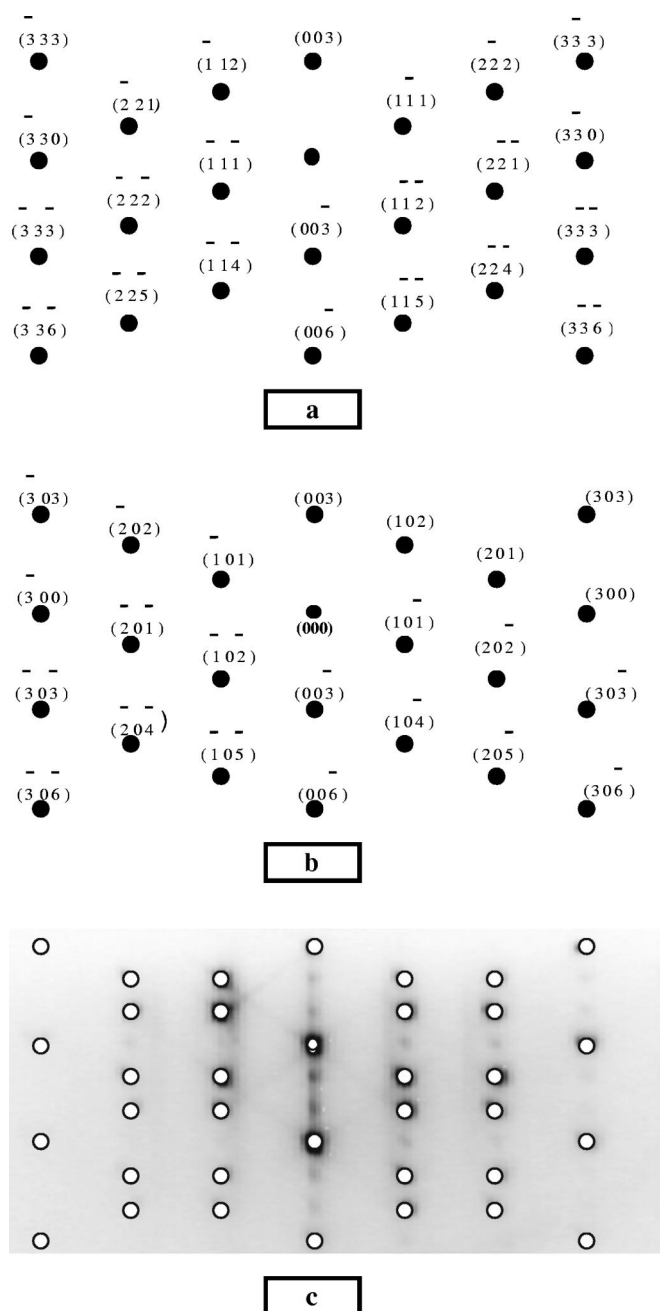


FIG. 5. Simulation of the diffraction patterns obtained by transmission across the  $60^\circ$  twinned nanoparticles. (a) Diffraction pattern along the  $[001]$  azimuth [in hexagonal  $(abc)$  notation]. (b) Diffraction pattern along the  $[110]$  azimuth,  $60^\circ$  rotated from  $[001]$ . (c) Superposition of the two preceding patterns and comparison with experimental diffraction pattern of Fig. 3(c). The residual spots are attributed to a double diffraction effect (see text).

tensity ratio of the O  $1s$  and V  $2p$  lines remains the same before and after the Eu evaporation (within 0.5%). This essential result is well explained by the growth of pure Eu islands on the O- $c(6 \times 2)$  reconstructed surface. Indeed, because the O  $1s$  and V  $2p$  lines correspond to nearly the same kinetic energy, their associated electron mean free paths are approximately the same, and thus the intensities of these two lines are equally affected by the presence of Eu islands. This scenario is the only one compatible with the constant ratio of the V and O signals; oxidation of the Eu nanoparticles must

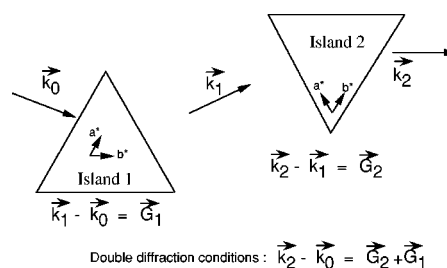


FIG. 6. Explanation of the low intensity spots of Fig. 3(c) by a double diffraction effect. The reciprocal lattice of island 2 is rotated by  $60^\circ$  compared to the reciprocal lattice of island 1, so that the  $\vec{G}_2$  vector has to be written in the reciprocal basis of island 1.

lead to a change of this ratio. In Figs. 7(b) and 7(c), a clear change of the O  $1s$  line shape (956 eV) is observed after the Eu evaporation. This indicates changes in the chemical bonding with oxygen, probably induced by the presence of Eu in contact.

Taking into account these conclusions, one can now use the crystallographic analogy between our oxygen free islands and the EuO oxide in order to build a qualitative understanding of the growth process. For this purpose, one has to remember that hexagonal EuO(111) planes are made of a succession of pure Eu planes and pure oxygen planes. Thus, the  $T_S$  value of  $260^\circ\text{C}$  needed for the observation of the Eu fcc phase can be interpreted as the temperature for which a Eu-O chemical reaction occurs, but it is restricted to the first deposited Eu atoms in contact with the  $c(6 \times 2)$  chemisorbed oxygen. As a consequence the first deposited Eu atoms form a hexagonal Eu(111) plane of the EuO type. Additional Eu deposits lead to the formation of 3D Eu fcc islands rather than bidimensional layers, because of strains induced by the drastic reduction (9.5%) of the Eu first-neighbor distance in this crystallographic phase.

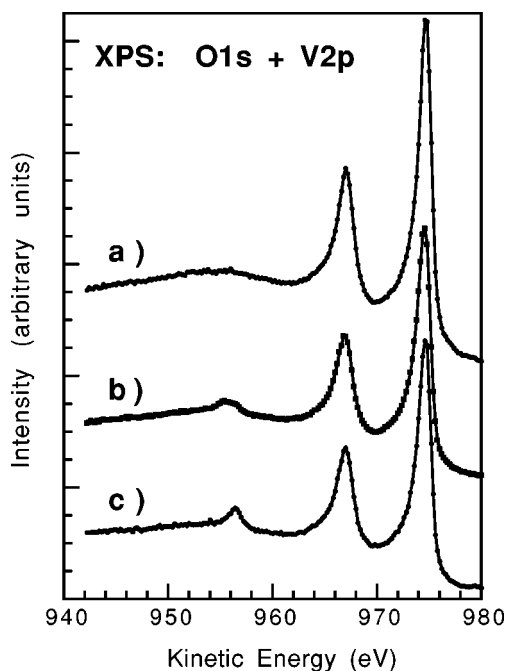


FIG. 7. (a) XPS V  $2p$  spectrum of the freshly ion bombarded V(110) surface. (b) Same spectrum for the  $S_{c(6 \times 2)}$  substrate. The O  $1s$  peak appears at 956 eV kinetic energy. (c) Same as (b) but after the evaporation of  $18 \text{ \AA}$  Eu.

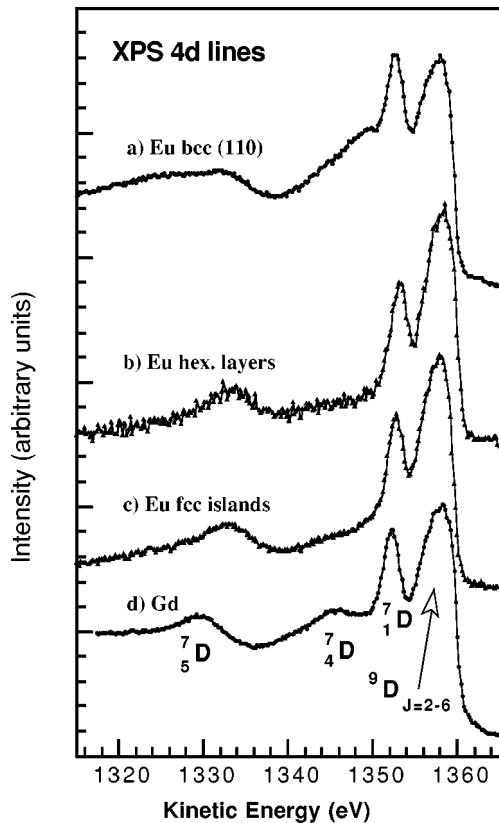


FIG. 8. Eu XPS spectra in the  $4d$  region of (a) Eu bcc (110) grown on V(110) at room temperature ( $100 \text{ \AA}$ ); (b) hexagonal Eu layers grown on V(110) at  $T_S=260 \text{ }^\circ\text{C}$ ; (c) fcc islands grown on the reconstructed  $O\text{-}c(6\times 2)$  V(110) surface at  $T_S=260 \text{ }^\circ\text{C}$ ; (d) hexagonal Gd layers grown on V(110) at  $T_S=300 \text{ }^\circ\text{C}$ . Note that for comparison this spectrum has been shifted by  $+12.4 \text{ eV}$ .

### B. Eu $4d$ photoemission

Typical Eu  $4d$  photoemission spectra are presented in Fig. 8. For comparison, a Gd  $4d$  spectrum obtained from a thick epitaxial layer on V(110) is also reported. As Gd metal is trivalent in the bulk ( $\text{Gd}^{3+}:4f^7$ ) while Eu is divalent ( $\text{Eu}^{2+}:4f^7$ ), the  $4f$  filling is the same for the two ions and thus the atomic description of core spectra must be similar. An early interpretation of these  $4d$  lines was done by Kowalczyk *et al.* in 1974.<sup>21</sup> The two main peaks lying at high kinetic energy originate from  $LS$  coupling between the open shells  $4d^9$  ( $^2D$ ) and  $4f^7$  ( $^8S$ ), giving rise to the two spectroscopic states  $^7D$  and  $^9D$ . The  $^9D$  indexing of the higher kinetic energy peak was later confirmed with high resolution XPS measurements on the EuTe compound, revealing the spin-orbit splitting of this state into five components  $^9D_J$  ( $J=2-6$ ).<sup>22</sup> The two bumps lying at lower kinetic energy have received attention only recently<sup>23,24</sup> in the case of Gd. We follow here the interpretation of van der Laan *et al.*,<sup>23</sup> which is supported by magnetic circular dichroism experiments on Gd(0001). Actually, at variance with the  $^9D$  state, the  $^7D$  can also be formed by coupling the  $4d^9$  ( $^2D$ ) state with five

parent terms of the  $f^7$  configuration. This gives rise to five eigenstates  $^7_kD$  ( $k=1-5$ ) well dispersed in energy and to the indexing quoted in Fig. 8. The two states  $^7_2D$  and  $^7_3D$  have very small intensities so that they can be neglected.

Returning to our experimental results and looking at Fig. 8, the main observation is the difference of shape between the usual Eu bcc  $4d$  line and the corresponding ones for both hexagonal Eu layers and fcc Eu islands. Clearly, this difference of shape cannot be explained in the framework of a simple atomic description and one must take into account the ion environment. Selås and Raaen invoked a strong substrate-adsorbate interaction in order to explain the differences they observed on the Eu  $3d$  spectra at the Eu/Ta interface.<sup>25</sup> The  $3d$  spectra we measured<sup>26</sup> in Eu/V show the same behavior. However, our spectra correspond to a few tens of ångströms in Eu thickness. This rules out the possibility of an electronic influence of the substrate on the photoemission line shapes. Actually, one has to find an explanation that takes into account the essential conclusions we can draw from our structural experiments. First, Eu  $4d$  spectra are structure dependent: hexagonal Eu layers give rise to a very different  $4d$  line shape when compared with bcc layers. Secondly, this difference cannot be due to a change of the first-neighbor distance. Indeed, this distance is very similar for the Eu bcc ( $3.97 \text{ \AA}$ ) and hexagonal ( $4.1\pm 0.1 \text{ \AA}$ ) layers, and, despite its large variation in the case of fcc Eu islands ( $3.59\pm 0.07 \text{ \AA}$ ), the spectra of Figs. 8(b) and 8(c) are similar. Thus, there is a possibility for the number of first neighbors to play an important role. The similarity between these spectra and the Gd  $4d$  one is in agreement with this assumption, because the common point to these three cases is the hexagonal stacking of the materials. This leads to the suggestion that the  $^7_kD$  states may be influenced by different crystal field effects, in spite of their weakness, whether Eu is in a bcc structure or a hexagonal one.

Changes of the Gd  $4d$  line shape have been recently reported<sup>27</sup> in Gd intermetallic compounds. This suggests band effects (due to structural changes) as another possible explanation. These suggestions will be discussed in detail elsewhere.<sup>26</sup>

### V. CONCLUSION

We have shown that 2D hexagonal Eu layers of a few tens of ångströms with  $a=4.1\pm 0.1 \text{ \AA}$  are obtained by Eu deposition on a pure  $(1\times 1)$ -V(110) substrate. In the presence of the oxygen induced  $c(6\times 2)$  surface reconstruction of V(110), 3D island growth of pure Eu is preferred for  $T_S=260 \text{ }^\circ\text{C}$ . The islands have the fcc structure with  $a_{\text{fcc}}=5.1\pm 0.1 \text{ \AA}$ . This implies a large reduction of the Eu first-neighbor distance when compared to the natural bcc phase. The fcc phase is made of Eu(111) planes of the EuO type, probably initiated by a chemical reaction between oxygen atoms lying in the  $c(6\times 2)$  reconstruction and the Eu atoms in contact. In both cases (2D and 3D growth), singular Eu  $4d$  spectra have been measured having very different line shapes when compared to the Eu bcc spectrum.

- \*Laboratoire de Physique des Matériaux is Unité Mixte de Recherche 7556 du Centre National de la Recherche Scientifique.
- <sup>1</sup>H. Brune, K. Bromann, H. Röder, K. Kern, J. Jacobsen, P. Stolze, K. Jacobsen, and J. Nørskov, *Phys. Rev. B* **52**, R14 380 (1995).
- <sup>2</sup>P. Bonanno, M. Canepa, P. Cantini, L. Mattera, R. Moroni, and S. Terreni, *Surf. Sci.* **454–456**, 697 (2000).
- <sup>3</sup>Gd, Tb, Dy, Ho, Er/W(110): H. Li, D. Tian, J. Quinn, Y.S. Li, S.C. Wu, and F. Jona, *Phys. Rev. B* **45**, 3853 (1992).
- <sup>4</sup>Sm/W(110): A. Ciszewski and A.J. Melmed, *J. Phys. (Paris), Colloq.* **45**, C9-39 (1984).
- <sup>5</sup>Ce/W(110): E. Vescovo and C. Carbone, *Phys. Rev. B* **53**, 4142 (1996).
- <sup>6</sup>Sm/Mo(110): A. Stenborg, J.N. Andersen, O. Björneholm, A. Nilsson, and N. Mårtensson, *Phys. Rev. Lett.* **63**, 187 (1989).
- <sup>7</sup>Y, Gd/Nb(110): J. Kwo, M. Hong, and S. Nakahara, *Appl. Phys. Lett.* **49**, 319 (1986).
- <sup>8</sup>Dy/V(110): K-Y. Yang, H. Homma, and I.K. Schuller, *J. Appl. Phys.* **63**, 4066 (1988).
- <sup>9</sup>Dy, Tb, Sm/Nb(110): C. Dufour, K. Dumesnil, and D. Pierre (private communication).
- <sup>10</sup>Ce/V(110): B. Kierren, T. Gourieux, F. Bertran, and G. Krill, *Phys. Rev. B* **49**, 1976 (1994).
- <sup>11</sup>Eu/W(110): J. Kolaczkiwicz and E. Bauer, *Surf. Sci.* **175**, 487 (1986).
- <sup>12</sup>Eu/Ta(110): C.G. Olson, X. Wu, Z.L. Chen, and D.W. Lynch, *Phys. Rev. Lett.* **74**, 1992 (1995).
- <sup>13</sup>P. Villars and L.D. Calvert, *Pearson's Handbook of Crystallographic Data for Intermetallic Phases* (American Society for Metals, Metals Park, OH, 1985), Vol. 3.
- <sup>14</sup>D.L. Adams and H.B. Nielsen, *Surf. Sci.* **107**, 305 (1981).
- <sup>15</sup>B. Kierren, T. Gourieux, F. Bertran, and G. Krill, *Appl. Surf. Sci.* **68**, 341 (1993).
- <sup>16</sup>C. Sürgers and H.V. Löhneysen, *Appl. Phys. A: Solids Surf.* **54**, 350 (1992).
- <sup>17</sup>More details will be given about this reconstruction in an independent paper.
- <sup>18</sup>Throughout this section, we use the hexagonal (*abc*) notation for the spot indexing as well as for crystallographic axes and azimuths.
- <sup>19</sup>See, for instance, D.W. Pashley and M.J. Stowell, *Philos. Mag.* **8**, 1605 (1963).
- <sup>20</sup>T.J. Konno, N. Ogawa, K. Wakoh, K. Sumiyama, and K. Suzuki, *Jpn. J. Appl. Phys., Part 1* **35**, 6052 (1996).
- <sup>21</sup>S.P. Kowalczyk, N. Edelstein, F.R. McFeely, L. Ley, and D.A. Shirley, *Chem. Phys. Lett.* **29**, 491 (1974).
- <sup>22</sup>D.A. Shirley, in *Photoemission in Solids I*, Vol. 26 of Topics in Applied Physics, edited by M. Cardona and L. Ley (Springer, Berlin, 1978), p. 172.
- <sup>23</sup>G. van der Laan, E. Arenholz, E. Navas, A. Bauer, and G. Kaindl, *Phys. Rev. B* **53**, 5998 (1996).
- <sup>24</sup>H. Ogasawara, A. Kotani, and B.T. Thole, *Phys. Rev. B* **50**, 12 332 (1997).
- <sup>25</sup>T.Ø. Selås and S. Raaen, *J. Phys.: Condens. Matter* **2**, 7679 (1990).
- <sup>26</sup>T. Gourieux *et al.* (unpublished).
- <sup>27</sup>J. Szade, J. Lachnitt, and M. Neumann, *Phys. Rev. B* **55**, 1430 (1997).